

AD-A175 515

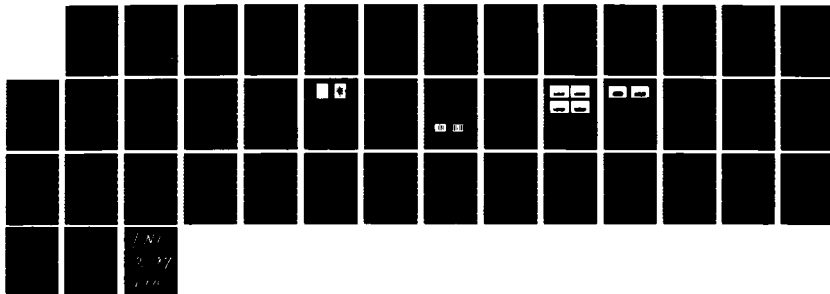
REAL TIME IMAGING WITH RADIO WAVES AND MICROWAVES(U)  
GENERAL DYNAMICS SAN DIEGO CA ELECTRONICS DIV  
G TRICOLES ET AL 30 AUG 86 R-86-016 ARO-22491 1-EL

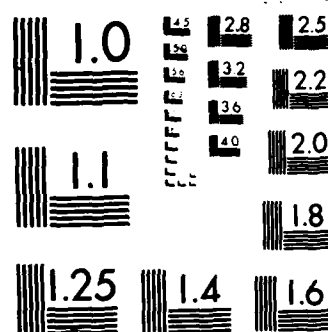
1/1

UNCLASSIFIED

F/G 17/9

NL





XEROCOPY RESOLUTION TEST CHART

AD-A175 515

DTIC FILE COPY

ARO 22491.1-EL

R-86-016  
30 August 1986

2

# REAL TIME IMAGING WITH RADIO WAVES AND MICROWAVES

Final Report

15 August 1985 thru 14 August 1986

G. Tricoles, E. L. Rope, J. L. Nilles

30 August 1986

U.S. ARMY RESEARCH OFFICE

ARO Project No. P-22491-EL  
Contract Number DAAG29-85-C-0024

Approved for Public Release  
Distribution Unlimited

DTIC  
ELECTE  
DEC 29 1986  
S A D

**GENERAL DYNAMICS**  
*Electronics Division*

R-86-016  
30 August 1986

# REAL TIME IMAGING WITH RADIO WAVES AND MICROWAVES

## Final Report

15 August 1985 thru 14 August 1986

G. Tricoles, E. L. Rope, J. L. Nilles

30 August 1986

U.S. ARMY RESEARCH OFFICE

ARO Project No. P-22491-EL  
Contract Number DAAG29-85-C-0024

Approved for Public Release  
Distribution Unlimited



**GENERAL DYNAMICS**

**Electronics Division**

P.O. Box 85227, San Diego, California 92138-5227 • 619-573-6111

Accession For	
NTIS GRA&I	<input checked="" type="checkbox"/>
DTIC TAB	<input type="checkbox"/>
Unannounced	<input type="checkbox"/>
Justification	
By	
Distribution/	
Availability Codes	
Dist	Avail and/or Special
A-1	

UNCLASSIFIED

SECURITY CLASSIFICATION OF THIS PAGE (When Data Entered)

AD-A175516

REPORT DOCUMENTATION PAGE		READ INSTRUCTIONS BEFORE COMPLETING FORM
1. REPORT NUMBER  ARO 22491.1-EL	2. GOVT ACCESSION NO.  N/A	3. RECIPIENT'S CATALOG NUMBER  N/A
4. TITLE (and Subtitle)  Real Time Imaging with Radio Waves and Microwaves		5. TYPE OF REPORT & PERIOD COVERED  Final Report - 8/15/85-8/14/86
		6. PERFORMING ORG. REPORT NUMBER
7. AUTHOR(s)  G. Tricoles, E. L. Rope, J. L. Niles		8. CONTRACT OR GRANT NUMBER(s)  DAAG29-85-C-0024
9. PERFORMING ORGANIZATION NAME AND ADDRESS General Dynamics Electronics Division P.O. Box 85227 San Diego, CA 92138-5227		10. PROGRAM ELEMENT PROJ. TASK AREA & WORK UNIT NUMBERS  N/A
11. CONTROLLING OFFICE NAME AND ADDRESS U. S. Army Research Office Post Office Box 12211 Research Triangle Park, NC 27709		12. REPORT DATE 30 August 1986
14. MONITORING AGENCY NAME & ADDRESS (if different from Controlling Office)		13. NUMBER OF PAGES
		15. SECURITY CLASS. (of this report)  Unclassified
		15a. DECLASSIFICATION/DOWNGRADING SCHEDULE
16. DISTRIBUTION STATEMENT (of this Report)  Approved for public release; distribution unlimited.		
17. DISTRIBUTION STATEMENT (of the abstract entered in Block 20, if different from Report)  NA		
18. SUPPLEMENTARY NOTES  The view, opinions, and/or findings contained in this report are those of the author(s) and should not be construed as an official Department of the Army position, policy, or decision, unless so designated by other documentation.		
19. KEY WORDS (Continue on reverse side if necessary and identify by block number)  Imaging, microwave, infrared, optical computing, parallel processing, inverse scattering		
20. ABSTRACT (Continue on reverse side if necessary and identify by block number)  An approach to real-time microwave holographic imaging was studied. In particular, spatially noncoherent wavefront reconstruction methods were evaluated theoretically, numerically, and experimentally.  Spatially noncoherent reconstruction is done by doubling holograms; that is by forming two axially symmetric replicas of -		

UNCLASSIFIED

SECURITY CLASSIFICATION OF THIS PAGE(When Data Entered)

an original hologram. Axially symmetric pairs of points are coherent but not coherent with other pairs.

Two theoretical descriptions of the reconstruction are given. One theory assumes a hologram is formed and computes image intensity of the doubled hologram on the basis of array theory for the region of Fraunhofer diffraction, the farfield. The other theory also computes farfield image intensity, but it describes hologram formation for a point object and reference source; this theory involves integration over continuous apertures rather than discrete point sources as in array theory. *f*

The continuous theory can be interpreted physically to predict image locations. Both theories predict image locations that agree with measurement, but the discrete theory predicts magnitudes that more closely agree with measured values.

Reconstruction experiments were done. No formation experiments were done to eliminate equipment costs; instead, previously formed holograms were used. The holograms were of a log periodic array radiating first in its sum mode and then in its difference mode. Wavelength was 3.30 cm.

Reconstructions were done with radiation of two distinct wavelengths.

Reconstructions were done with coherent infrared radiation from a line array of four  $0.85\mu\text{m}$  solid-state lasers, which replicated the hologram intensities. Holograms were doubled by directing the output of a laser to a pair of optical fibers. Reconstruction intensity was measured by an array of charge-coupled devices.

Reconstructions were also done with 8.57 mm waves. A pair of waveguides was connected to a signal generator. Interference fringe intensity was separately measured for four spacings of the radiating ends of the waveguides by scanning the image region with a small receiving antenna. The intensity for each spacing was stored in a computer and intensities for the four spacings were summed to effect noncoherent superposition.

The  $0.85\mu\text{m}$  reconstructions were described better by the discrete theory rather than the continuous; image locations were correct for both, but second-order image intensity was more accurate for the discrete theory. The continuous theory described the magnitudes of the millimeter wave reconstruction better than did the discrete theory. The apparent reason is in the width of hologram fringes compared to widths of radiation sources. That is, the element factor enters.

UNCLASSIFIED

SECURITY CLASSIFICATION OF THIS PAGE(When Data Entered)

## CONTENTS

<u>Section</u>		<u>Page</u>
	OVERVIEW, BACKGROUND, AND BRIEF SUMMARY .....	0-1
1	INTRODUCTION .....	1-1
2	SPATIALLY NONCOHERENT WAVEFRONT RECONSTRUCTION .....	2-1
3	EXPERIMENT: FIBER OPTIC, INFRARED HOLOGRAM DOUBLER ...	3-1
4	THEORY: DISCRETE, RADIATING SOURCES .....	4-1
5	THEORY: CONTINUOUS, SEPARATED APERTURES .....	5-1
6	ALTERNATIVE RECONSTRUCTION METHODS .....	6-1
7	MILLIMETER WAVE SPATIALLY NONCOHERENT RECONSTRUCTION .....	7-1
8	SUMMARY .....	8-1
9	REFERENCES .....	9-1

## ILLUSTRATIONS

<u>Figure</u>	<u>Title</u>	<u>Page</u>
1	Spatially Noncoherent Wavefront Reconstruction for Long Wavelength Holography. T is a transmitting antenna. $T_R$ is a reference wave antenna. The object O was a letter F. A is an array of receiving antennas. B is an array of light sources. D is a doubler, explained in Figure 2. The image is at I. ....	2-1
2	A Hologram Doubler. H is a hologram. S is a beam splitter. P is a prism. DH is the doubled hologram. ....	2-2
3	Computer-Generated Hologram of Letter F ....	2-2
4	Coherent Light Reconstructions from Scale-Reduced Hologram of Figure 3. For B the exposure was longer than for A. ....	2-3
5	First Seven Frames of Film Strip for Sequential Exposure ....	2-3
6	Spatially Noncoherent Reconstruction Produced by Sequential Exposure of Film Strip in Figure 5. ....	2-3
7	Fiber Optic Doubler with Charge-Coupled Device (CCD) Detector Array ....	3-1
8	Apparatus for Forming Microwave Holograms of Log-Periodic Antenna (LPA). A is a receiving antenna; D a detector; S an oscilloscope; SG a signal generator; $T_R$ an antenna that radiates the reference wave. ....	3-2
9	Holograms of Antenna. In A the antennas of the LPA radiated in phase; in B, out of phase. ....	3-2
10	Experimental Arrangement of Fibers in Hologram Doubler. The outer circles represent the claddings; the inner the cores. ....	3-3
11	Brightness Distributions for Reconstructions. A shows fiber input end arrangement. B shows input brightness for sum mode, and C is brightness at output of doubler. D shows input brightness mode for difference, and E is at output of doubler. ....	3-3
12	Intensity Fringes. Fiber pair spacings: A, 78 $\mu\text{m}$ ; B, 232 $\mu\text{m}$ ; C, 398 $\mu\text{m}$ ; D, 530 $\mu\text{m}$ . Vertical scale is 50 mV per square. ....	3-4



# ILLUSTRATIONS (Continued)

<u>Figure</u>	<u>Title</u>	<u>Page</u>
13	Reconstruction Intensity for Log Periodic Array. A is for the antennas radiating in the sum mode; B is for the difference mode. ....	3-5
14	Coordinates for Reconstruction. Sources are at $(0, \pm Y_m)$ . The observation point P is assumed in the array's farfield. ....	4-1
15	Reconstruction Intensity Calculated from Equation 2. The upper graph is for the sum mode; the lower for the difference. ....	4-3
16	Formation Step Geometry .....	5-2
17	Coordinates for Integration Over Doubled Holograms .....	5-3
18	Reconstruction Intensity from Equation 17 for $M = 795$ , $a = 150 \mu m$ , $W = 150 \mu m$ .....	5-6
19	Reconstruction Intensity from Equation 17. $M = 795$ ; $a = 150 \mu m$ ; $W = 120 \mu m$ .....	5-7
20	Reconstruction Intensity from Equation 17, for $M = 795$ ; $a = 190 \mu m$ ; $W = 150 \mu m$ .....	5-7
21	Real Time Holographic System with Coherent Reconstruction $R_i$ through $R_N$ 10 GHz intensity receivers; $R_S$ is a radiating source at 15 GHz; $M_1$ through $M_2$ are p-i-n diode modulators; L is a lens. ....	6-1
22	Intensity from Two Metallic Waveguides Spaced 17.8 cm at 48 cm Distance for Wavelength 8.57 mm .....	7-2
23	Reconstructed Intensity Produced by Summing Intensities for Four Spacings of Metallic Waveguide Pair .....	7-2
24	Intensity from Two Dielectric Waveguides Spaced 17.8 cm at 48 cm Distance; Wavelength 8.57 cm .....	7-2
25	Intensity Produced by Summing Intensities for Four Spacings of Dielectric Waveguide Pair .....	7-2

## OVERVIEW, BACKGROUND, AND BRIEF SUMMARY

This report describes a new technique that accelerates long wavelength holography, which utilizes radiation with wavelengths in the range of millimeters to hectameters. Only electromagnetic waves are considered, but applications to acoustics seem possible.

### Background On Holography

Holography is an imaging method that involves two steps.

In the first, a coherent beam illuminates an object, which scatters a wave onto a detector. A second wave propagates directly from source to detector, interacting negligibly or not at all with the object. The second wave, the reference wave, propagates around the object or on a distinct path. The two waves interfere, producing an intensity pattern that is recorded. In the beginning of holography, Gabor utilized visible radiation, and the detector was photographic film. The developed film was called a hologram to emphasize that both phase and intensity were recorded by intensity measurements. This first step is called *hologram formation*; it can be considered data acquisition.

The second step produces images. For example, in the case of visible light, a hologram illuminated with a coherent beam scatters a wave proportional to the object wave. This step is called *wavefront reconstruction*; it can be considered data processing.

Holographic imaging differs significantly from photography and conventional imaging with lenses. Holographic images have three dimensional structure, unlike photographs. The two step process permits spatial filtering for image enhancement. Holography produces images of objects obscured by diffusing layers, unlike conventional imaging. In addition, holograms are directly useful, for they show spatial phase distributions of object-scattered waves.

## Long Wavelength Holography

Experiments have shown that long wavelength holography is feasible for many, diverse applications. Most of the experiments were done in laboratories with standard equipment rather than specially developed systems. A notable and highly developed counter-example is synthetic aperture radar, which can be interpreted in terms of holography. In general though, the potential applications require continued research on understanding, accelerating, and simplifying long wavelength holography.

Long wavelength holography has two somewhat overlapping kinds of applications. One is identifying objects; the other is diagnostic.

Identification includes problems like those in radar, where one or more objects are to be detected and classified or identified. Compared to long wavelength holography, radar is well developed. For example, airborne synthetic aperture radar produces images of terrain. The coordinates of these images are distance and one transverse dimension because data are synthesized in range by the radar pulse and in cross-range by aircraft motion.

In contrast, holographic images have two transverse coordinates if two dimensional antenna arrays are used. However, holographic images with one radial coordinate have been produced without pulsed radiation by superimposing a sequence of images that were reconstructed from a series of one dimensional holograms. References give details.

Another distinction between radar and long wavelength holography is that holographic systems can passively form images. That is, a radiating source can be imaged. The reference wave can be extracted by a separate receiving antenna.

Long wavelength holography is appropriate for identifying objects obscured by regions that attenuate or scatter visible light. For example, propagation through the terrestrial atmosphere distorts conventional images. Objects buried in soil or snow have been identified in microwave holographic experiments. Geological applications include the imaging of geological faults from holograms synthesized by flying aircraft that receive waves from ground-based radio transmitters.

Diagnostic applications include studying radiation by antennas and propagation through radomes. Multipath propagation has been studied. Three examples are microwave scattering by radomes, the troposphere, and water waves. The multipath studies show that useful holograms result naturally from the configuration of propagation paths.

### Methods of Long Wavelength Holography

Despite its feasibility, long wavelength holography remains rather slow, and image quality is, in most cases, rather low. This section describes reasons for this situation as a preliminary to describing our research.

Low image quality, in comparison to visible images, results in part from low resolution produced by apertures with dimensions that are comparable to the wavelength. However, subwavelength resolution has been obtained from semicircular holograms and from overlapping images from sequences of holograms synthesized by an aircraft. Other factors affecting image quality will be described later in this section.

Speed is usually low in laboratory experiments with general-purpose apparatus. Specialized apparatus can greatly accelerate long wavelength holography; of course, costs are a restriction. Speed is more than a convenience; it is important for imaging transient events or sequences of transient events. Moreover, speed is essential in applying imaging to the control of robots or vehicles that identify obscured objects such as buried land mines.

To see how speed and image quality depend on procedures and apparatus, let us consider early methods of long wavelength holography. In early work the hologram fringe pattern was sampled by translating an antenna over an area, which was approximately perpendicular to the object scattered wave. The detected intensity was displayed on an oscilloscope and photographed. The photograph was scale-reduced to produce a hologram. Images were generated by illuminating the hologram with a laser beam.

This procedure was slow, of the order of minutes, partly because the probe was mechanically scanned and because a tangible hologram was produced. Scanning delays have been reduced, to two seconds, with crossed arrays of receiving antennas that sequentially received and transmitted; with a receiver of each array, the data acquisition

delays can be reduced by an order or magnitude. An array that spans an area can further reduce scanning delays.

Another delay was in producing a tangible hologram. This delay has been reduced by digitally computing images. With a dedicated computer, delays can be on the order of seconds; the sources of delay are analog-to-digital conversion, computation, and display of images.

Digital computation also improves image quality by eliminating the scale-reduced hologram and its laser illumination. These holograms usually were not reduced in the scale of visible and nonvisible wavelengths because of the limited resolution of cameras. Consequently, images were small and longitudinally distorted.

#### Inverse Scattering: The General Setting of Long Wavelength Holography

Long wavelength holography is a special case of inverse scattering.

Inverse scattering is a name given to a wide group of physical and mathematical problems that involve wave scattering and have as solutions, or goals, information about the configuration or composition of a scattering object. The known data include the diffracted field, which is the sum of the incident and scattered fields; in addition, if the illuminating source is controlled, the incident field is known at the scatterer and at the observation point. Inverse problems differ from direct problems, which start with data on the object and incident field and have scattered fields as solutions. Direct problems are analytic; inverse problems synthesize scatterer properties.

Inverse scattering problems are diverse. In physics, an early example is the study of atomic structure with beams of electrons and alpha particles. More recently, inverse problems have been considered in quantum scattering theory. In engineering, radar problems motivate research on electromagnetic inverse scattering to identify objects or determine properties of propagation paths. The synthesis of antennas and layered dielectrics are additional examples. In medicine, X-ray tomographic imaging is widely accepted; tomography is also done with acoustic waves.

In addition to tomography, inverse scattering includes other forms of imaging. An example is determining the relationships between objects and blurred images in optical instruments. Holographic imaging also has been described in terms of inverse scattering, by Porter and Devaney, who showed that real image formed by a wave converging from a closed hologram is proportional to the complex conjugate of the minimum energy source that generated the hologram. Imaging by synthetic aperture radar also has a holographic interpretation.

Clearly, inverse scattering is a unifying general concept that includes many applications that are done with diverse instruments in a wide spectrum of temporal frequencies for both acoustic and electromagnetic waves.

### Problems Treated in this Report

This report describes a new method for accelerating long wavelength holography. In particular, it describes an approach to real-time wavefront reconstruction. It gives theoretical analyses and experimental verification. It excludes experiments on hologram formation because scope is limited; however, results are given for processing of existing holograms.

### Summary

This report describes a method for real-time wavefront reconstruction. The method is a form of optical computing. In particular it is parallel processing and can be described as wavefront processing because the data propagate through the system like a wave. This description is more than analogy; the incoming long wave is replicated as a shorter wave and then optically processed. The processor has no memory and thus requires no clock; however, images can be stored.

The method involves doubling the hologram, that is, producing two axially symmetric holograms from the original. A doubling device is, for example, an array of solid-state lasers; each is connected to a pair of optical fibers, which are arranged to produce the axially symmetric pair of holograms. The output ends of the fibers radiate producing Fourier transforms of the holograms and hence images. The novel aspect here is that

radiation from axially symmetric pairs of fibers interferes, but interference does not occur between waves from distinct pairs. Thus, considerations of spatial coherence underlie the approach.

Experimental confirmation is given. By starting with existing microwave (9.3 GHz) holograms of log-periodic antennas, we produced images of their active regions for sum and difference modes. Images were formed at wavelength 0.85 micrometer. Additional measurements were made with a doubler that used 8.57 millimeter waves.

## 1. INTRODUCTION

Experiments show that holography with microwaves and radio waves is feasible and useful for many, diverse applications that include the identification of scatterers, analysis of propagation through the terrestrial atmosphere, and diagnostics of antennas and radomes (see References 1-11). Although holography is most often done with visible light, the microwave and radio wave versions are useful because the longer wavelengths penetrate regions opaque to visible light, are inherent in the operation of antennas and radomes, and give resonant scattering for objects of appropriate sizes. In addition, long wavelength holograms often occur as consequences of propagation, rather than in deliberate laboratory experiments; examples are multiple propagation paths in the troposphere or radomes.

Long wavelength holography is useful for two reasons. First, it produces images, which help in identifying objects or interpreting scattering phenomena. Images assist human observers and may be useful for automatic interpretation by machines. The second reason is that holograms are interferograms for diagnostics of scattering or of radiation by antennas and radomes.

The applications of long wavelength holography are examples of inverse scattering, which provides a unifying theoretical framework; however, the diversity of the applications generates distinct and specialized techniques for data acquisition and processing. Apparatus is highly developed for some applications; for example, synthetic aperture radar, which has a holographic interpretation, produces detailed terrain images from moving aircraft or orbital satellites (References 12-14). In contrast, techniques are rather slow and inconvenient for some potential applications such as imaging transient events or identifying buried objects from robots. Some progress has been made recently in special cases such as testing large reflector antennas (Reference 15) and airborne bistatic imaging of geological features (Reference 16). In general, fast and convenient techniques seem lacking for long wavelength holography.



Time delays occur in both data acquisition, or measurement, and in data processing, or computation; both apparatus and procedures cause delays.

In early measurements, data were acquired in the hologram formation step by scanning an antenna over an area to measure the intensity of a fringe pattern or the complex-valued object wave. The measured data were encoded by photographing and scale reducing an oscilloscope display to produce a hologram transparency. The encoded data were processed, in the reconstruction step, by illuminating the transparency with a coherent beam of visible light.

Antenna arrays of crossed configuration have reduced acquisition delays, and digital computers have reduced processing delays. Computational reconstruction also eliminates image degradation that results if holograms are not scaled by the ratio of the formation and reconstruction wavelengths because of limited camera resolution.

The acquisition delays can be virtually eliminated by using specialized instrumentation. Antenna arrays would eliminate scanning an antenna over an area. A receiver at each receiving antenna eliminates delays caused by switching a single receiver. The use of these techniques is limited by the cost of a system, not by technology.

The processing delays occur in analog-to-digital conversion, in sequential computation even with Fourier transform algorithms for imaging, and in displaying the image data, say on a cathode ray tube presentation.

The processing delays are the problem that was studied in the research project described by this report.

This report describes a method for real-time reconstruction from long wavelength hologram data. The method is optical and parallel, a form of wavefront processing (References 17 and 18); it is spatially noncoherent. The next section describes the method. Subsequent sections describe two theoretical descriptions as well as measurements and computations for  $0.85\text{ }\mu\text{m}$  radiation. A section compares reconstruction methods; it refers to an earlier coherent method that utilized centimeter waves. Another section describes spatially noncoherent reconstruction with  $8.57\text{ mm}$  waves. A final section summarizes results of the study.

## 2. SPATIALLY NONCOHERENT WAVEFRONT RECONSTRUCTION

Figure 1 shows an approach to real time, long wavelength holography based on spatially noncoherent reconstruction. A transmitting antenna illuminates the object, and a second antenna radiates a reference beam. The object and reference beams are received by an array of antennas, at A. Each antenna is connected to a detector that responds to intensity in the interference pattern. The intensity detected by each detector is displayed by a set of separately coherent light sources at B. The display produces a scale-reduced replica of the long wavelength interference pattern. A one-to-one correspondence exists between the set of receiving antennas and coherent sources. Although each light source is coherent, no two sources are mutually coherent. The fringe pattern at B is a hologram. Two replicas of the hologram are produced by propagation through a doubler (defined in Figure 2), and further propagation, possibly through a lens, produces holographic images (as suggested in Figure 1).

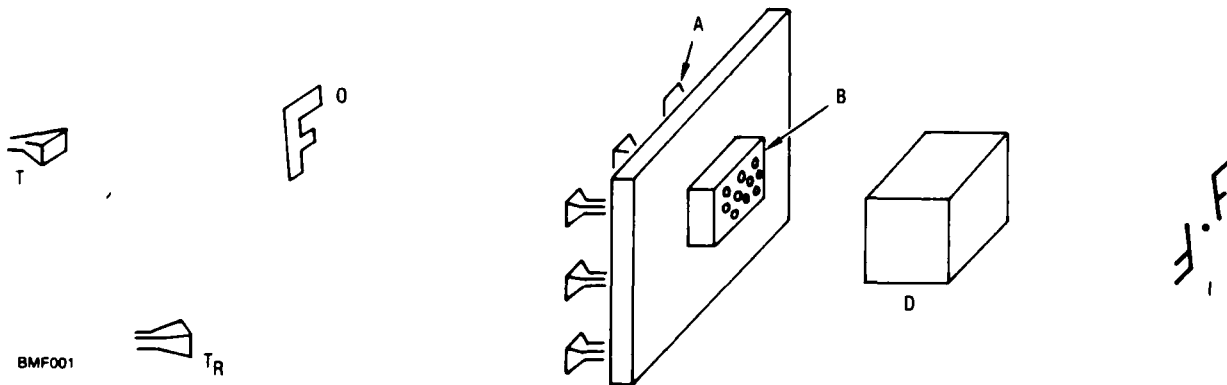


Figure 1. Spatially Noncoherent Wavefront Reconstruction for Long Wavelength Holography. T is a transmitting antenna. T<sub>R</sub> is a reference wave antenna.

The object O was a letter F. A is an array of receiving antennas. B is an array of light sources. D is a doubler, explained in Figure 2.

The image is at I.

A doubler D produces two axially symmetric holograms. Figure 2 shows a possible embodiment. It consists of a beam splitter and two prisms with orthogonal orientations. The light from a source in one hologram is coherent with the light at an axially symmetric source in the other hologram but is not coherent with light from nonaxially

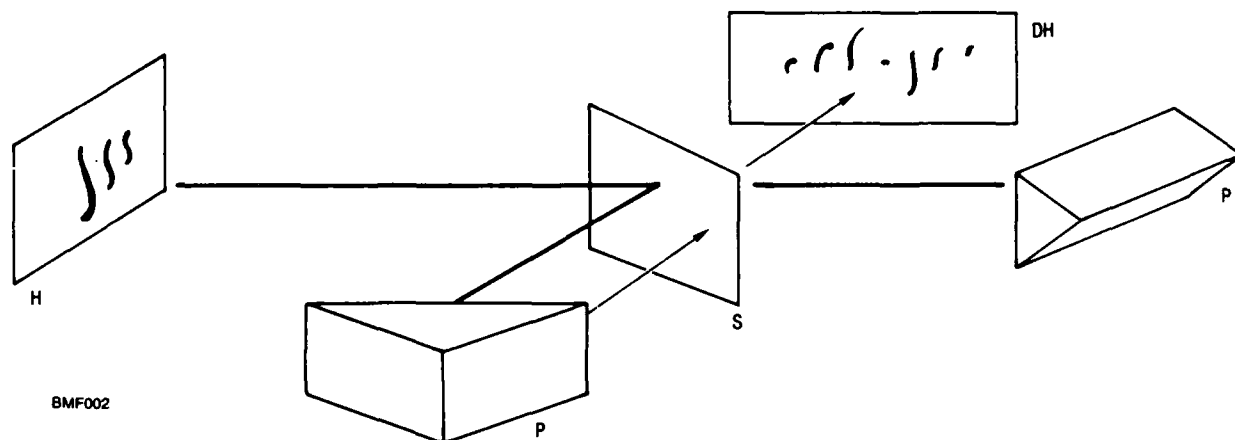


Figure 2. A Hologram Doubler. H is a hologram. S is a beam splitter. P is a prism. DH is the doubled hologram.

symmetric points. Of course, the sources in either hologram are separately coherent but not mutually coherent. This arrangement is the reason for the name spatially noncoherent.

The feasibility of spatially noncoherent reconstruction was demonstrated by a simulation experiment to avoid the expense of the array and doubler in Figures 1 and 2. The object was planar, the letter F. A detour phase hologram (Reference 19) was prepared and verified by illuminating it with a coherent beam of 6328 Å light. The hologram is shown in Figure 3, and the image in Figure 4. A spatially noncoherent reconstruction was done by forming a sequence of apertures in a film strip. The apertures were axially symmetric pairs; Figure 5 shows the first seven frames of the strip. Note that the first frame contains one aperture, which is the central aperture of the hologram in Figure 3.

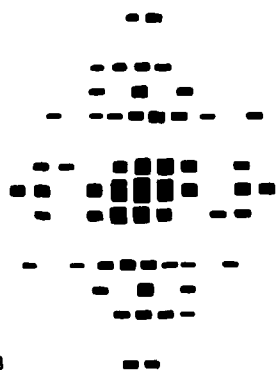
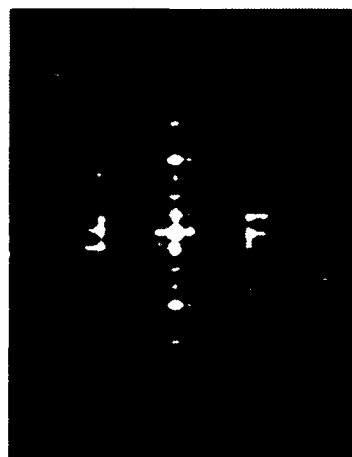


Figure 3. Computer-Generated Hologram of Letter F



BMF004

A



B

Figure 4. Coherent Light Reconstructions from Scale-Reduced Hologram of Figure 3. For B the exposure was longer than for A.

Thus the doubled holograms were separated by zero distance. Spatially noncoherent reconstruction was done by illuminating a frame, opening a shutter to expose recording film, and sequentially exposing all frames. In this way, the intensities from the exposures add, giving spatially noncoherent reconstruction. Figure 6 shows the spatially noncoherent reconstruction.



BMF005

Figure 5. First Seven Frames of Film Strip for Sequential Exposure



BMF006

Figure 6. Spatially Noncoherent Reconstruction Produced by Sequential Exposure of Film Strip in Figure 5.

### 3. EXPERIMENT: FIBER OPTIC, INFRARED HOLOGRAM DOUBLER

The interferometer in Figure 2 is conceptually simple, but it is delicate, unsuitable for field use. Therefore, we fabricated a doubler that uses an array of laser diodes and a pair of optical fibers from each laser. Figure 7 shows the lasers and fibers, with a Charge-Coupled Device (CCD) array as a detector. The lasers operated with continuous radiation at 0.85 micrometer wavelength. The core diameters were 6 micrometers; cladding outside diameter was 75 micrometers. The fibers were arranged in a horizontal line, and they were all adjacent. The CCD array has 256 detectors, each spaced by 25 micrometers. Distance from the radiating ends of the fibers to the CCD array was 105 mm. The output of the CCD array was presented on an oscilloscope fitted with a Polaroid camera.

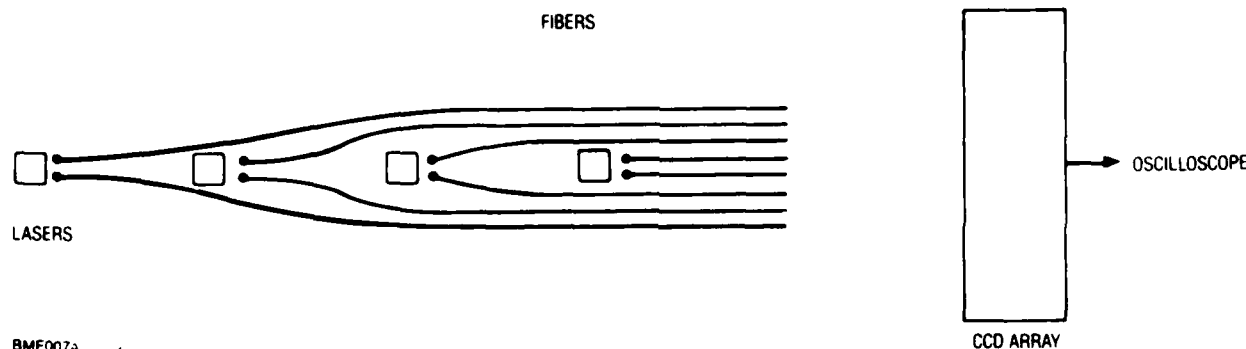


Figure 7. Fiber Optic Doubler with Charge-Coupled Device (CCD) Detector Array

Experiments were done without an antenna array; instead, existing holograms were utilized. The holograms were formed with the setup in Figure 8. A 9.100-GHz microwave source was connected to an array of two Log Periodic Antennas (LPAs) and through a directional coupler (equivalent to a beam splitter) to a horn antenna  $T_R$  that radiated the reference beam. The antennas were coplanar and  $T_R$  was 0.55m from the LPA. The intensity on a plane 1.00 meter from the plane containing the LPA and  $T_R$  was scanned by moving a small receiving antenna over a region of the plane. The angle between the object and reference beams was approximately  $29^\circ$ . Detected intensity was recorded by photographing the oscilloscope display.

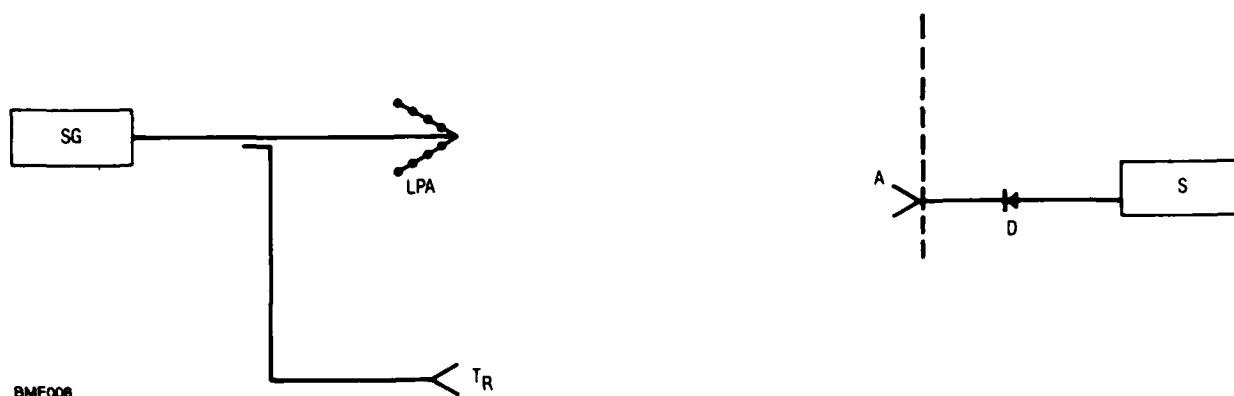


Figure 8. Apparatus for Forming Microwave Holograms of Log-Periodic Antenna (LPA).  
 A is a receiving antenna; D a detector; S an oscilloscope; SG a signal generator;  
 $T_R$  an antenna that radiates the reference wave.

The log periodic array can radiate in two modes. In one, the sum mode, both antennas radiate in phase. In the other mode the two antennas radiate out of phase. Figure 9 shows microwave holograms formed for the sum and difference modes.

Because we utilized only four lasers, only four hologram intensity peaks were represented and only for a horizontal section of the holograms. Figure 10 shows the arrangement of fibers in the doubler. The outsides of adjacent pairs were in contact, giving approximate spacings between fiber centers of 75 micrometers. To represent the sum mode hologram of Figure 9a, the lasers were adjusted to give equal output. To represent the difference mode hologram, in Figure 9b, the central pair of lasers was extinguished, and the outer pair gave equal output. Figure 11 suggests the intensity distributions.



Figure 9. Holograms of Antenna. In A the antennas of the LPA radiated in phase; in B, out of phase.

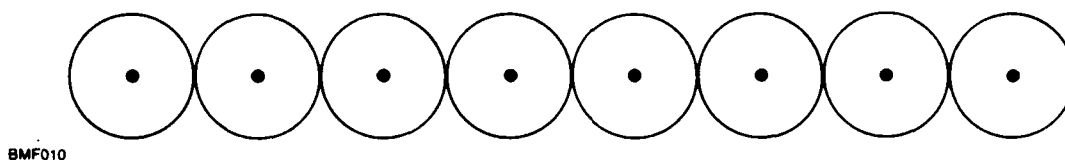


Figure 10. Experimental Arrangement of Fibers in Hologram Doubler.  
The outer circles represent the claddings; the inner the cores.

The fringe patterns formed at the CCD array were measured to test the setup. Figure 12 shows intensity measured when only one laser was on, and thus when only one of the fiber pairs radiated. The fringes show that coherence is obtained and the fringe spacings correlate well with those expected from the pair spacings of 75, 225, 375, and 525 microns.

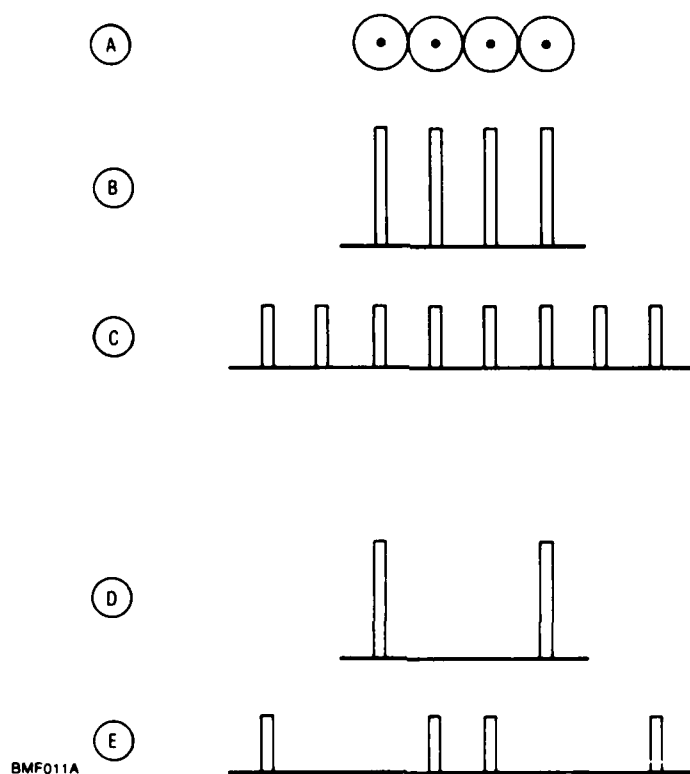


Figure 11. Brightness Distributions for Reconstructions. A shows fiber input end arrangement. B shows input brightness for sum mode, and C is brightness at output of doubler. D shows input brightness for difference mode, and E is at output of doubler.

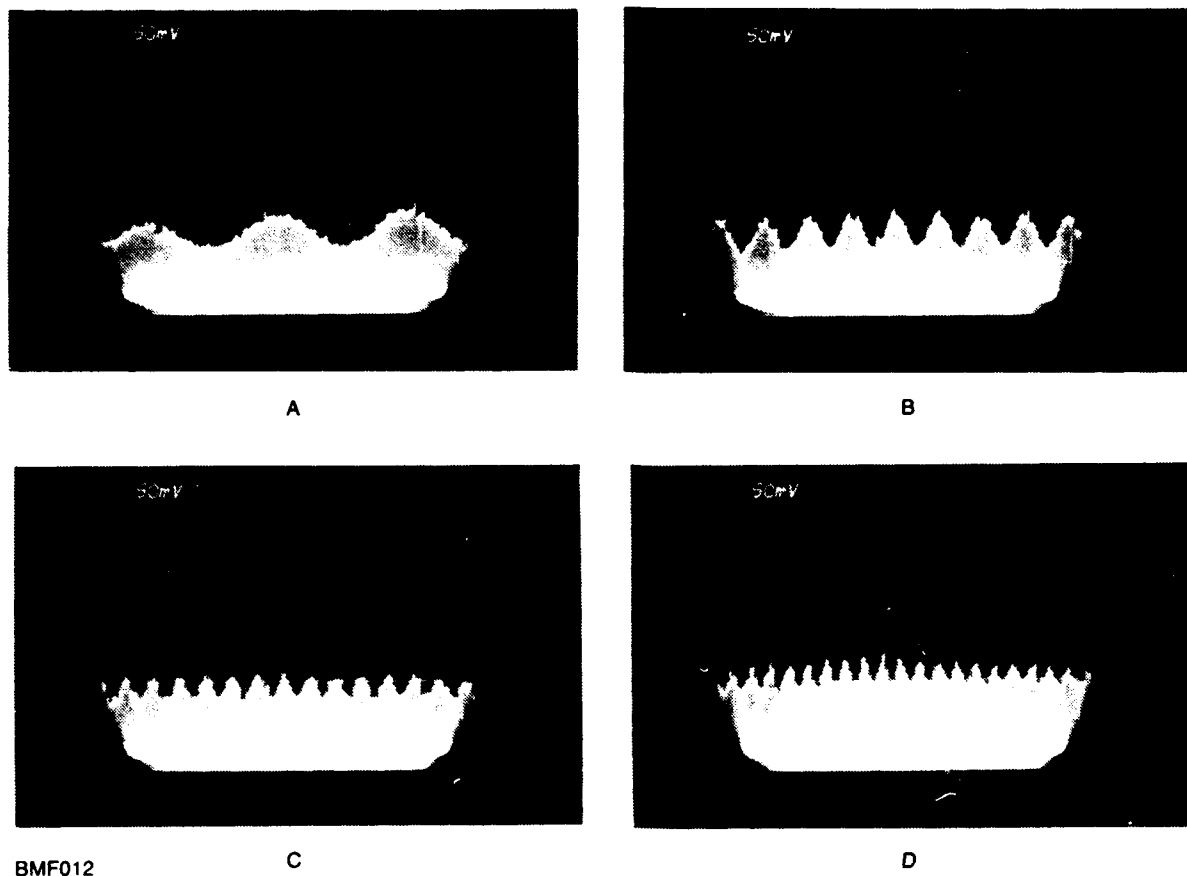
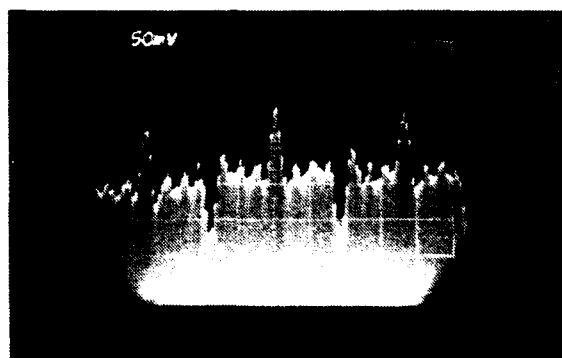


Figure 12. Intensity Fringes. Fiber pair spacings: A,  $78 \mu\text{m}$ ; B,  $232 \mu\text{m}$ ; C,  $398 \mu\text{m}$ ; D,  $530 \mu\text{m}$ . Vertical scale is 50 mV per square.

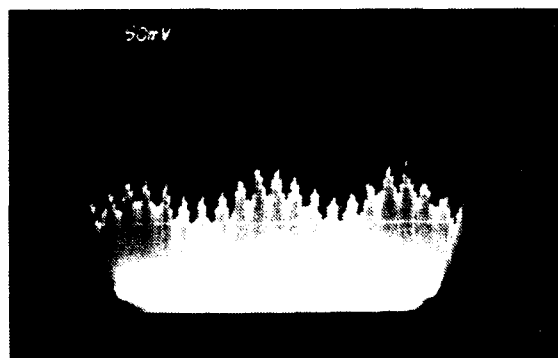
The reconstruction for the sum mode hologram of Figures 9a and 11a is shown in Figure 13a. The reconstruction for the difference mode (Figures 9b and 11b) is shown in Figure 13b. In Figure 13a, the high maxima outside the central order are images of the antenna. In Figure 13b, the pair of maxima at the locations of the maxima for the sum mode are images of the two elements of the array. The out-of-phase elements are resolved, but the in-phase elements are not. It is significant for interpretation that the sum mode and difference mode images occur at the same off-axis positions. Actually the outer large maxima in Figure 13a are second order images. The first orders are expected at the minima in Figure 13a. The next theoretical section predicts image locations and explains the missing orders.





BMF013

A



B

Figure 13. Reconstruction Intensity for Log Periodic Array. A is for the antennas radiating in the sum mode; B is for the difference mode.

#### 4. THEORY: DISCRETE, RADIATING SOURCES

To describe images let us consider the radiating ends of the fibers to be represented by an array of point sources as in Figure 14. This assumption ignores the diffraction pattern of the individual fibers so it is restricted to small angles off the axis normal to the plane containing the fiber ends. For a plane of constant  $x$  in the farfield or Fraunhofer region, antenna array theory gives for the amplitude from two, coherent, in-phase, equal amplitude point sources,

$$u_m = A_m (e^{ik'_y d_m} + e^{-ik'_y d_m}), \quad (1)$$

$$= 2A_m \cos(k'_y d_m)$$

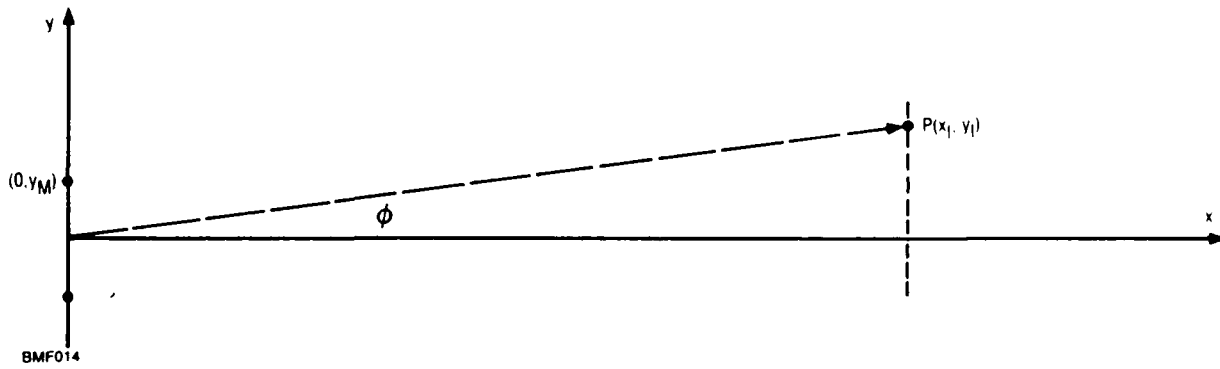


Figure 14. Coordinates for Reconstruction. Sources are at  $(0, \pm Y_m)$ . The observation point  $P$  is assumed in the array's farfield.

where  $A_m$  is the source amplitude,  $k'_y$  is  $(2\pi/\lambda') \sin \phi$ ; and  $\lambda'$  is the reconstruction wavelength,  $d_m$  is the distance of either source from the  $x$  axis of Figure 14, and  $\phi$  is the off axis angle. The intensity from the two sources is  $|u_m|^2$ . For an array of  $M$  pairs, where  $N$  is an integer, noncoherent addition of intensities gives image intensity.

$$|u_I|^2 = 4 \sum_{m=1}^M A_m^2 \cos^2(k'_y d_m) \quad (2)$$

The intensity given by Equation 2 was calculated for the sum and difference mode holograms of Figure 9 represented by the brightness distributions of Figure 11. That is, for the sum mode, the  $A_m$  all had unit value; for the difference mode,  $A_1$  and  $A_4$  had unit value, but  $A_2$  and  $A_3$  had value zero. The distances  $d_m$  were determined from fringe spacings in Figure 12. The values were 39, 116, 194, and 265 micrometers. If all cladding outside diameters were 75 micrometers, as given by the fiber manufacturer, these values would be 38, 113, 188, and 263 micrometers. The differences between the expected and experimental values of  $d_m$  are small and attributed to tolerances and possibly to an adhesive that restrained the fibers near their input ends.

Results of calculations are given in Figure 15. These computed values should be compared with the measured image intensities shown in Figure 13. The calculated values agree closely with the measured. The agreement exists despite the axial distance being only 105 mm and the usual  $(2d_m)/\lambda'$  criterion (for the farfield) being approximately 300 mm for the largest value of  $d_m$ ; of course  $(2d_m)^2/\lambda'$  has smaller values for those fibers closer to the x-axis.

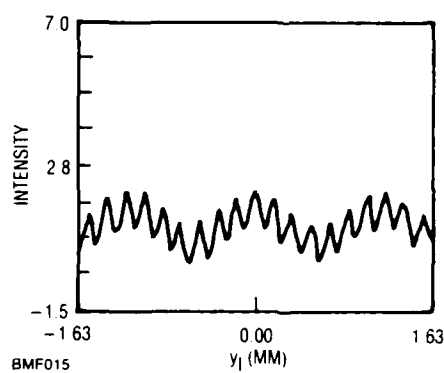
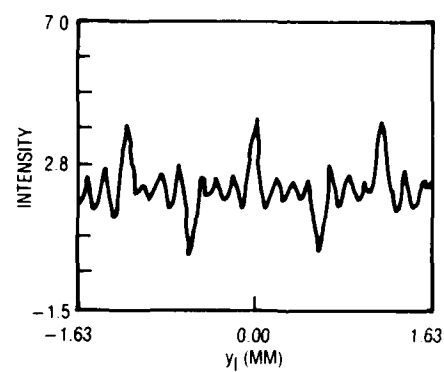


Figure 15. Reconstruction Intensity Calculated from Equation 2. The upper graph is for the sum mode; the lower for the difference.

## 5. THEORY: CONTINUOUS, SEPARATED APERTURES

Although the theory of the preceding section led to accurate calculations of reconstructed intensity, it omitted the formation step. The theory assumes the configuration of the shorter wavelength hologram is given. It omits the scale reduction between the formation and reconstruction steps; it also omits the formation wavelength, which differs from that for reconstruction. The theory does not provide a physical interpretation of intensity maxima as images.

This section presents an approximate diffraction theory that includes both the formation and reconstruction steps.

The formation step is described in Figure 16. A point object is assumed at the origin, and a point reference source at  $(0, y_r)$ . The situation is assumed two-dimensional. A receiving probe antenna measures intensity in the plane at  $x_h$  as a function of  $y_h$ . The scalar field, with wave polarization omitted, in the plane  $x_h$  is

$$u_h = \exp i k r_1 + \exp i (k r_2 + \alpha) \quad (3)$$

where  $\alpha$  is a constant phase adjustment that describes path differences, and, to quadratic approximations,

$$r_1 = x_h + (y_h^2 / 2x_h), \quad (4)$$

$$r_2 = x_h + [(y_h - y_r)^2 / 2x_h] \quad (5)$$

The hologram intensity is

$$|u_h|^2 = 4 \cos^2 \left[ (\pi y_r / 2\lambda x_h)(2y_h - y_r) - (\alpha / 2) \right] \quad (6)$$

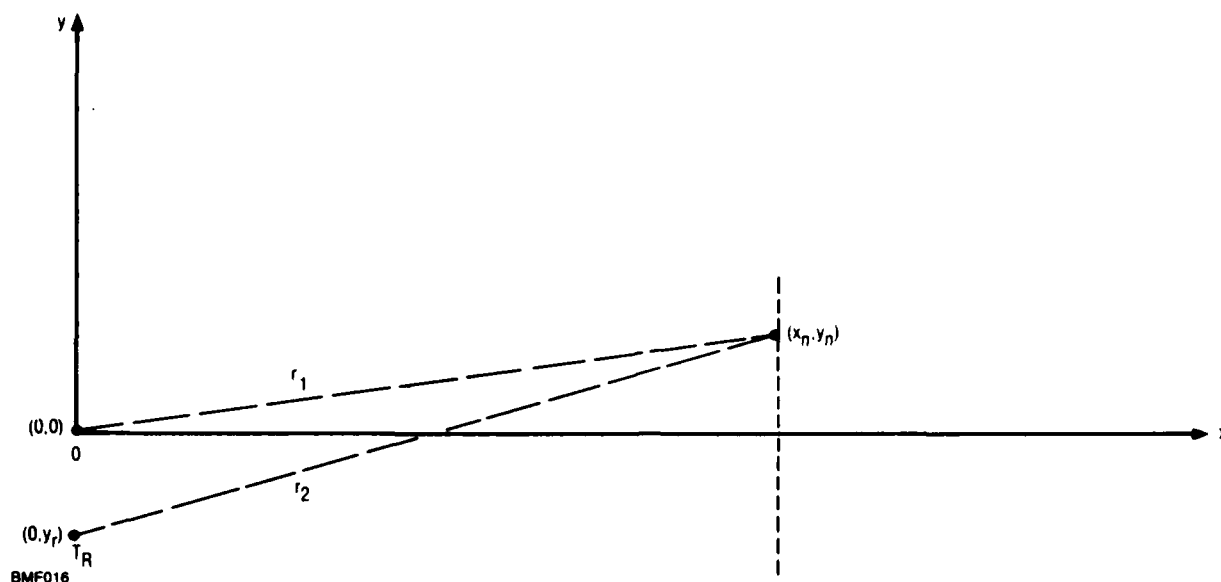


Figure 16. Formation Step Geometry

The value of  $\alpha$  adjusts the position of the fringes. In Figure 9, the intensity is a minimum for  $y_h$  having values near zero. Thus we set  $\alpha$  equal to  $\alpha'$  such that

$$-(2N + 1) \pi = (\pi y_r^2 / \lambda x_h) + \alpha' \quad (7)$$

where  $N$  is an integer, positive or negative. With  $\alpha'$ , Equation 6 gives

$$|u_h|^2 = 4 \sin^2 \delta y_h \quad (8)$$

where  $\delta$  is  $(y_r / \lambda x_h)$ ; this distribution is assumed over a finite width. To double the hologram as suggested by Figure 2, it is first shifted by distance  $a$ , so it is centered at  $y_h$  equal to  $a$ , and scale reduced by factor  $m$ ; the intensity in the fringe region is

$$|u_h|_+^2 = 4 \sin^2 [\delta m (y_h - a)] \quad (9)$$

The second axially symmetric hologram is obtained by inversion of  $y_h$  (substitute  $-y_h$  in Equation 9). It is centered at  $y_h$  equals  $-a$ . Because the  $\sin^2$  function is even, the second holograms intensity is

$$|u_h|_-^2 = 4 \sin^2 [\delta m (y_h + a)] \quad (10)$$

Figure 17 shows the arrangement of the two holograms. The upper hologram, centered at  $y_h$  equal to  $a$ , spans the region  $a - W \leq y_h \leq a + W$ . The lower hologram, centered at  $y_h$  equal to  $-a$ , spans the region  $-a - W \leq y_h \leq -a + W$ .

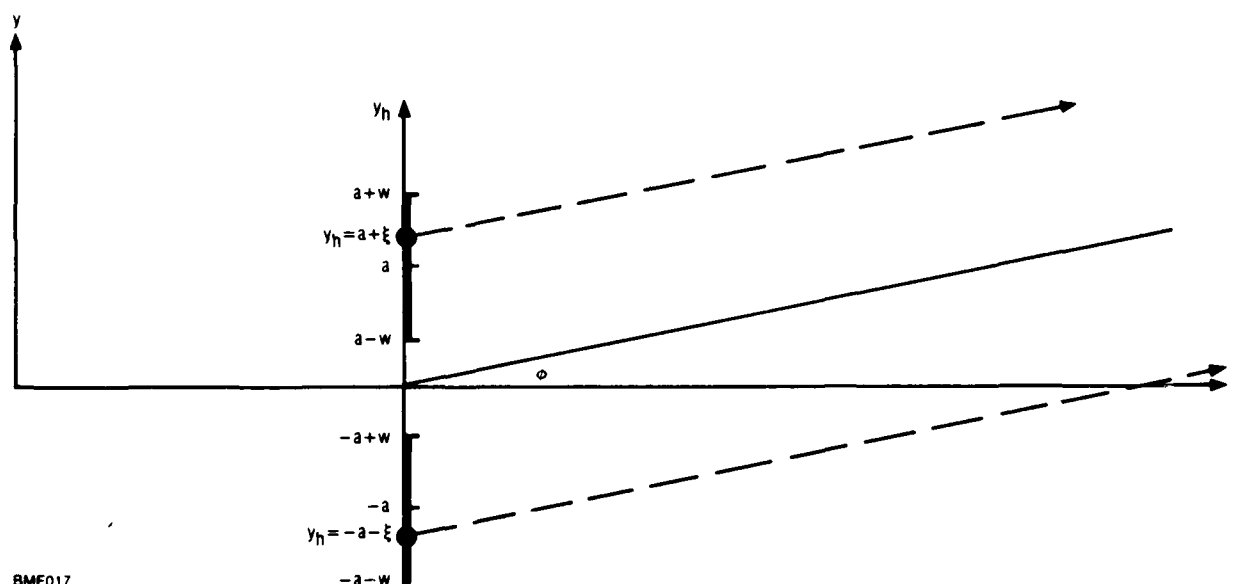


Figure 17. Coordinates for Integration Over Doubled Holograms

To evaluate image intensity, assume each point on the holograms is a radiating source with wavelength  $\lambda'$ . The source at a fixed value of  $y_h$  in the first hologram is coherent with the source at  $-y_h$  in the second hologram. Therefore, the complex-valued amplitude from two sources, at  $\pm y_h$ , is the complex sum of their complex amplitudes. This sum is, with  $k'$  equal to  $2\pi/\lambda'$  and omitting the factor  $\exp ik'R$ , where  $R$  is farfield distance,

$$u_i = |u_h|_+^2 \exp (-ik' y_{h+} \sin \phi) + |u_h|_-^2 \exp (-ik' y_{h-} \sin \phi) \quad (11)$$

where the notation  $y_{h+}$  emphasizes that the first term is for the upper hologram, where  $y_h$  is positive;  $y_{h-}$  in the second term for the lower hologram is negative. Image intensity is obtained by integrating  $|u_I|^2$  over all sources; intensities  $|u_I|^2$  add because only axially-symmetric points (at specific magnitudes of  $\pm y_h$ ) are mutually coherent.

To facilitate the integration, introduce the variable  $\xi$ , such that for symmetric points at  $\pm y_h$ , the value of  $y_h$  is  $a + \xi$  in the upper hologram, and  $y_h$  is  $-(a + \xi)$  in the lower. When  $\xi$  increases,  $y_h$  increases in the upper hologram but decreases in the lower. With the substitutions,  $y_{h+}$  equal to  $(a + \xi)$  in Equation 9 for the upper hologram, and  $y_{h-}$  equal to  $-(a + \xi)$  in Equation 10 for the lower, Equation 11 gives

$$\begin{aligned} u_i &= 4 \sin^2(\delta m \xi) \exp[-ik'(a + \xi) \sin \phi] + 4 \sin^2(\delta m \xi) \exp[ik'(a + \xi) \sin \phi] \\ &= 8 \sin^2(\delta m \xi) \cos[k'(a + \xi) \sin \phi] \end{aligned} \quad (12)$$

because the sine function squared is even valued. The intensity produced by two axially symmetric points is, with  $\sigma = k' \sin \theta$ ,

$$|u_i|^2 = 64 \sin^4(\delta m \xi) \cos^2[k'(a + \xi) \sin \phi] \quad (13)$$

The image intensity produced by adding intensities from all points in the hologram is

$$|u_I|^2 = \int_{a-w}^{a+w} |u_i|^2 d\xi \quad (14)$$

where  $2W$  is the width of the integration region.

To evaluate Equation 14, rewrite the integrand of Equation 13 with trigonometric identities to reduce the exponents of the trigonometric functions. An intermediate step gives

$$\begin{aligned} |u_I|^2 &= 8 \int_{a-w}^{a+w} (1 + \cos 2\delta m \xi + \cos^2 2\delta m \xi) [1 + \cos 2\sigma(a + \xi)] d\xi \\ &\quad - 32 \int \cos 2\delta m \xi [1 + \cos 2\sigma(a + \xi)] d\xi \end{aligned} \quad (15)$$



Further simplification gives

$$|u_I|^2 = 4 \int \left[ 3 + 3 \cos 2\sigma(\xi + a) - 4 \cos 2\delta m \xi + 4 \cos 4\delta m \xi \right. \\ \left. - 4 \cos 2\delta m \xi \cos 2\sigma(a + \xi) + \cos 4\delta m \xi \cos 2\sigma(a + \xi) \right] d\xi \quad (16)$$

The integrals involving products of cosines are simplified by expanding the cosines in exponential functions. The final result is

$$|u_I|^2 = 24W + 24W \cos(2\sigma a) \text{sinc}(2\sigma W) - 32W \text{sinc}(2\delta m W) \\ + 8W \text{sinc}(4\delta m W) - 16W \left\{ \text{sinc} \left[ 2W(\delta m + \sigma) \right] \right. \\ \left. + \text{sinc} \left[ 2W(\delta m - \sigma) \right] \right\} \cos 2\sigma a + 4W \left\{ \text{sinc} \left[ 2W(2\delta m + \sigma) \right] \right. \\ \left. + \text{sinc} \left[ 2W(2\delta m - \sigma) \right] \right\} \cos 2\sigma a \quad (17)$$

where  $\text{sinc } x = x^{-1} \sin x$ .

Inspection of Equation 17 gives some physical properties of images. The first, third, and fourth terms are independent of the angle  $\phi$ , giving uniform intensity. In the second term, the factor  $\text{sinc } 2\sigma W$  has maximum value on the x-axis, where  $\sigma$  has value zero. In the fifth and sixth terms, the factors  $\text{sinc} [2W(\delta m \pm \sigma)]$  have maxima for  $\sigma = \pm \delta m$ ; these would be images. In the seventh and eighth terms, the factors  $\text{sinc} [2W(2\delta m \pm \sigma)]$  have maxima where  $\sigma = \pm 2\delta m$ ; these would be second order images.

For the experimental conditions leading to Figure 13, for which  $m$  has value 795, from the condition  $\sigma$  equals  $\pm \delta m$ , we expect images at angle  $\phi$  equal to 0.00572 radian so the off axis distance  $y$  is 0.60 mm. The measured value is  $0.60 \pm 0.01$  mm, from the spacing of 24-1/2 picture elements in Figure 13; where elements are spaced by 25 micrometers. However, the intensity in Figure 13a has a minimum at the expected location of the image. (This minimum also occurred in Figure 15a for the discrete array theory.)

The factor  $\cos 2\sigma a$  explains the missing image. For the maximum conditions  $\sigma$  equals  $\pm \delta m$ ,  $\cos(2\sigma a)$  has unit value because  $(2\sigma a)$  is  $4\pi$  for  $m$  equals 795,  $a$  equals 150 micrometers, and  $\delta$  equals  $\pi y_r / \lambda' x_h$  with  $y_r$  equals -0.555m,  $\lambda$  equals 3.30 cm, and  $x_h$  equals 1.00 meter. When  $\cos(2\sigma a)$  has unit value, the term with the factor  $-16W$  in Equation 17 subtracts intensity from the image. An intensity minimum results.

The second order image gives a peak because for  $\sigma$  equal to  $\pm 2\sigma_m$ ,  $\cos 2\sigma a$  also has unit value because  $2\sigma a$  has value  $8\pi$ . The term with factor  $4W$  adds to the image intensity. An intensity maximum results.

Computations of  $|u_I|^2$  from Equation 17 are shown in Figures 18 through 20. For  $a$  equals 150 micrometers, Figures 18 and 19 have minima where the first order images are expected, in agreement with the measurements in Figure 13. However, the magnitude of the first order image can be increased by increasing  $a$ , as shown by Figure 20. The second order images have smaller magnitudes than those measured (Figure 13) or computed with the discrete array theory (Figure 15) although locations coincide with those measured and those computed from array theory. The explanation apparently is that the fringes given by Equations 9 and 10 are broader than the widths of the radiating ends of the fibers. Physically, each fringe regarded as a radiator has directional properties that tend to collimate the beam; this collimation is apparently less for the smaller radiating ends of the fibers than for the fringes in the continuous theory.

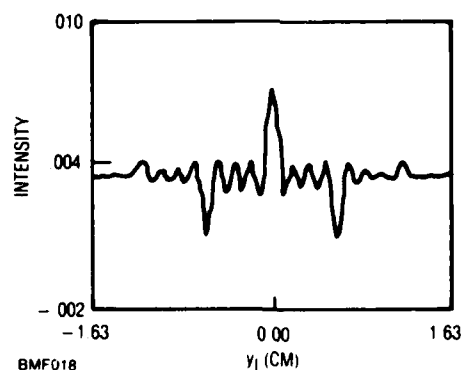


Figure 18. Reconstruction Intensity from Equation 17 for  $M = 795$ ,  
 $a = 150 \mu\text{m}$ ,  $W = 150 \mu\text{m}$

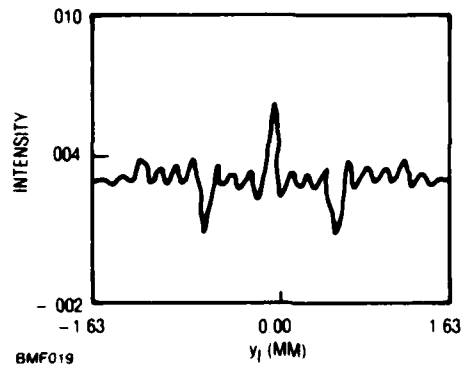


Figure 19. Reconstruction Intensity from Equation 17.  
 $M = 795$ ;  $a = 150 \mu\text{m}$ ;  $W = 120 \mu\text{m}$

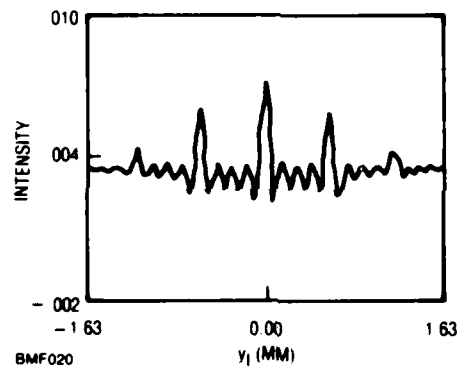


Figure 20. Reconstruction Intensity from Equation 17,  
for  $M = 795$ ;  $a = 190 \mu\text{m}$ ;  $W = 150 \mu\text{m}$

## 6. ALTERNATIVE RECONSTRUCTION METHODS

Wavefront reconstruction can be done in many ways. The purpose, speed, convenience, and equipment costs influence the choice.

One factor that distinguishes methods is coherence. Coherent radiation is normally used; in this case reconstruction can be experimental, an analog computation or numerical by digital computer. Spatially noncoherent reconstruction is relatively new.

Another factor is the wavelength of the reconstruction beam. Visible light permits human interpretation of images. CCD arrays also are convenient, when connected to an oscilloscope, for a range of infrared wavelengths. However, reconstruction can be done at longer wavelengths such as millimeter waves. Longer wavelengths ease component tolerance, and they reduce the ratio of formation to reconstruction wavelength.

An experimental real-time microwave holographic system has been developed (see Reference 18). The system included a receiving array that operated at 3 cm wavelength; coherent reconstruction was at 2 cm wavelength. See Figure 21.

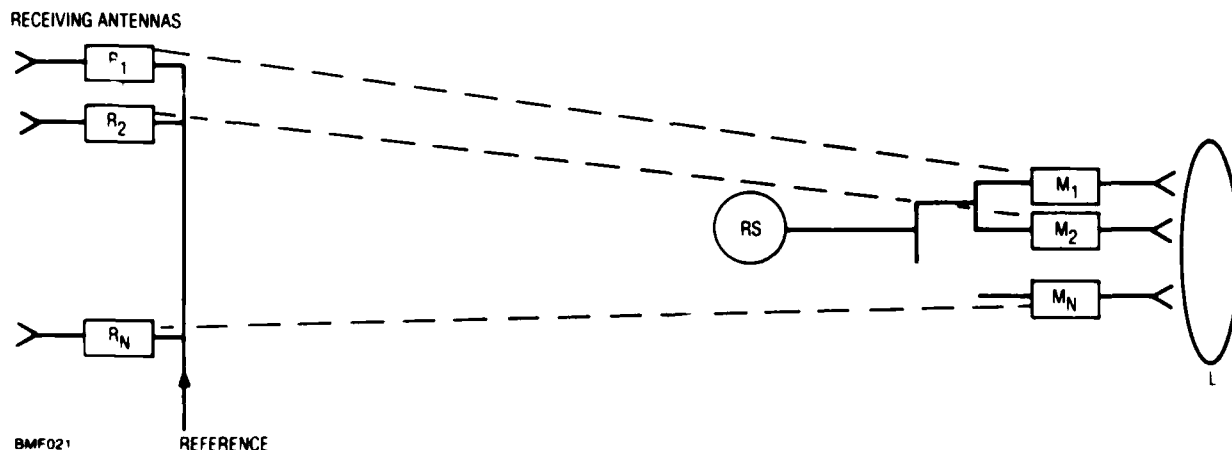


Figure 21. Real Time Holographic System with Coherent Reconstruction  
 $R_1$  through  $R_N$  10 GHz intensity receivers;  $R_S$  is a radiating source at 15 GHz;  $M_1$  through  $M_N$  are p-i-n diode modulators;  $L$  is a lens.

The next section describes a reconstruction experiment that used 35-GHz waves. Reconstruction was spatially noncoherent.

It seems too early to compare coherent and spatially noncoherent reconstruction methods for radio and microwaves. However, factors would be image quality and cost. Cost will be influenced by components for each architecture. In Figure 21, we have one reconstruction source, several p-i-n modulators, and a corporate feed which is one to many couplers. In Figure 9, for example, we have many sources but a simpler branching network.

## 7. MILLIMETER WAVE SPATIALLY NONCOHERENT RECONSTRUCTION

Reconstructions were done at 35 GHz, wavelength 8.57 millimeter, approximately  $10^4$  times the wavelength of the laser radiation described earlier.

The apparatus resembled that in Figure 7, but it was less extensive and of course utilized millimeter wave components. The source was a laboratory signal generator. It was connected to a pair of flexible waveguides.

Two distinct kinds of waveguide were used in separate experiments. One pair was a flexible, metallic wound, hollow rectangular waveguide, which was connected to the signal generator through a waveguide T-section. The other pair was dielectric. One end of each was inserted into the generator's output port, where they touched. The rods and pipes were separated gradually toward their open radiating ends.

Two distinct experiments were done: one with the dielectric waveguides; the other with the wire-wound pipes. To simulate the array of four sources and four pairs of fibers (as in Figure 7), the radiating ends of the waveguides were placed at each of four pairs of positions. Spacings were 2.5, 7.5, 12.7, and 17.8 cm, roughly 3, 9, 15, and 21 wavelengths. Intensity was measured for each pair position by translating a small receiving antenna, connected to a detector, on a line 48 cm from the plane of the receiving apertures. The intensities for each of the four spacings of the radiating apertures were stored in a computer, and then the intensities were summed. The summed intensities are images.

For the experiment with flexible metallic waveguides, Figure 22 shows intensity fringes for the largest spacing, 17.8 cm. Figure 23 shows the sum of intensity for the four waveguide aperture spacings. This sum corresponds to  $|u_I|^2$  in Equation 2. In Figure 22, the minima at  $y$ , approximately  $\pm 8$  cm spacing, correspond to the deep minima in Figure 13a. The low maxima at  $y$ , approximately  $\pm 16$  cm, correspond to the second-order images. These images have lower intensity relative to the zero order, receiving antenna, and the radiating apertures. The fringes in Figure 22 show a strong decrease with lateral displacement.

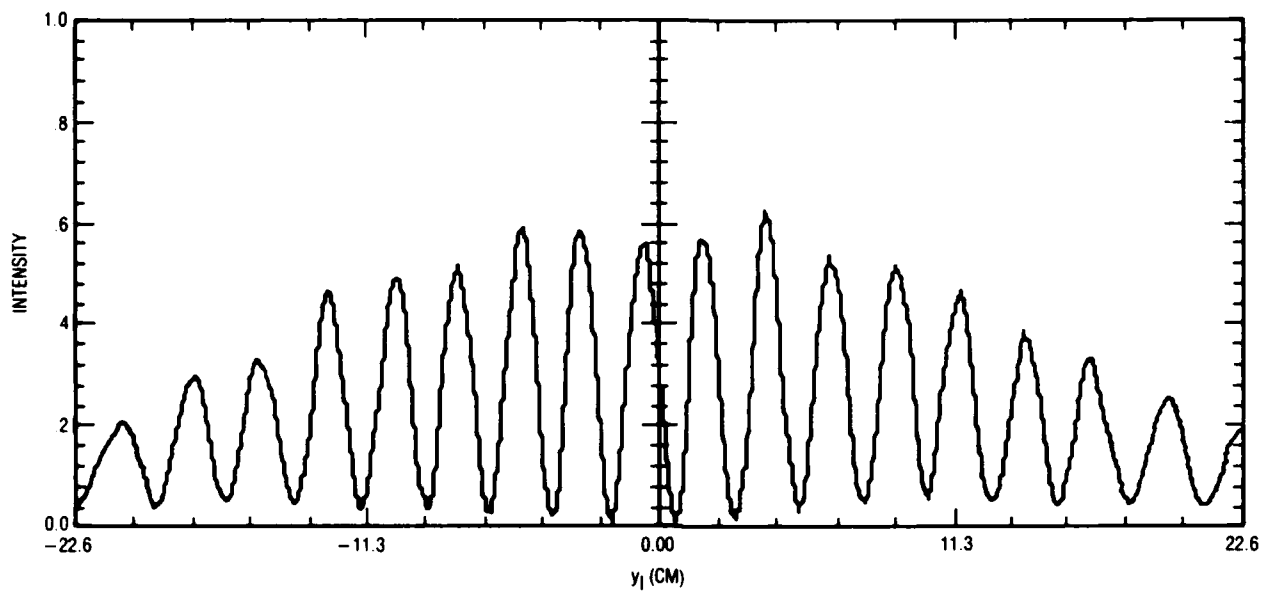


Figure 22. Intensity from Two Metallic Waveguides Spaced  
17.8 cm at 48 cm Distance for Wavelength 8.57 mm

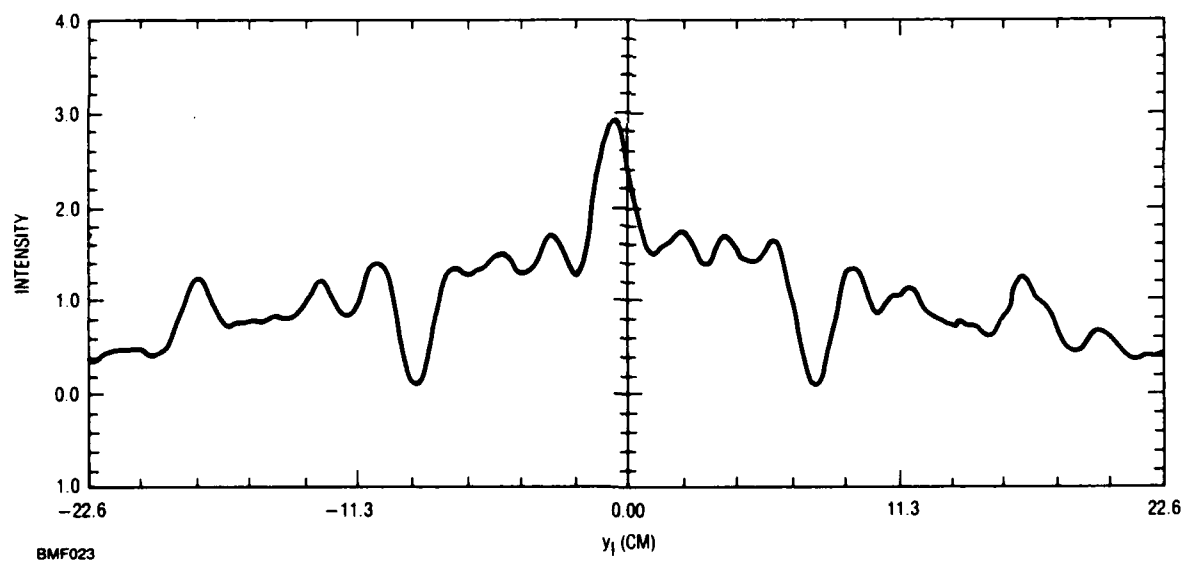


Figure 23. Reconstructed Intensity Produced by Summing  
Intensities for Four Spacings of Metallic Waveguide Pair

For the experiment with dielectric waveguides, Figure 24 shows intensity of fringes again for the largest spacing of 17.8 cm. The intensity decreases with later displacement more rapidly for the dielectric waveguides than it does for the metallic. Figure 25 shows the reconstructed image intensity. The second-order images seem less distinct than those for the metallic waveguide setup; see Figure 23.

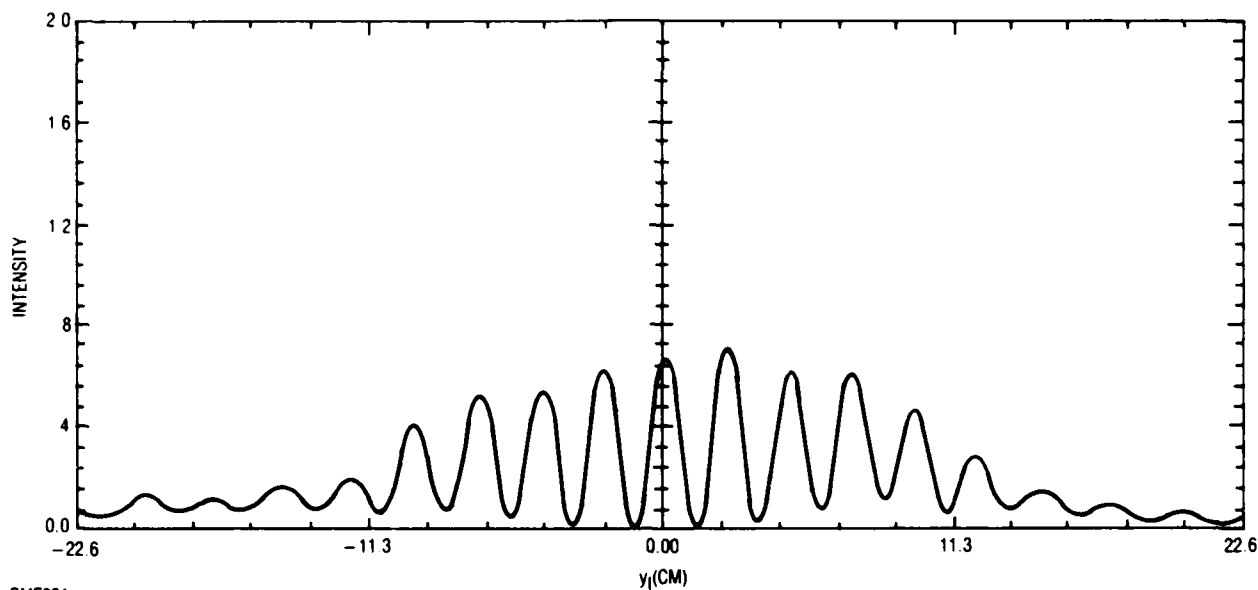


Figure 24. Intensity from Two Dielectric Waveguides Spaced 17.8 cm at 48 cm Distance; Wavelength 8.57 cm

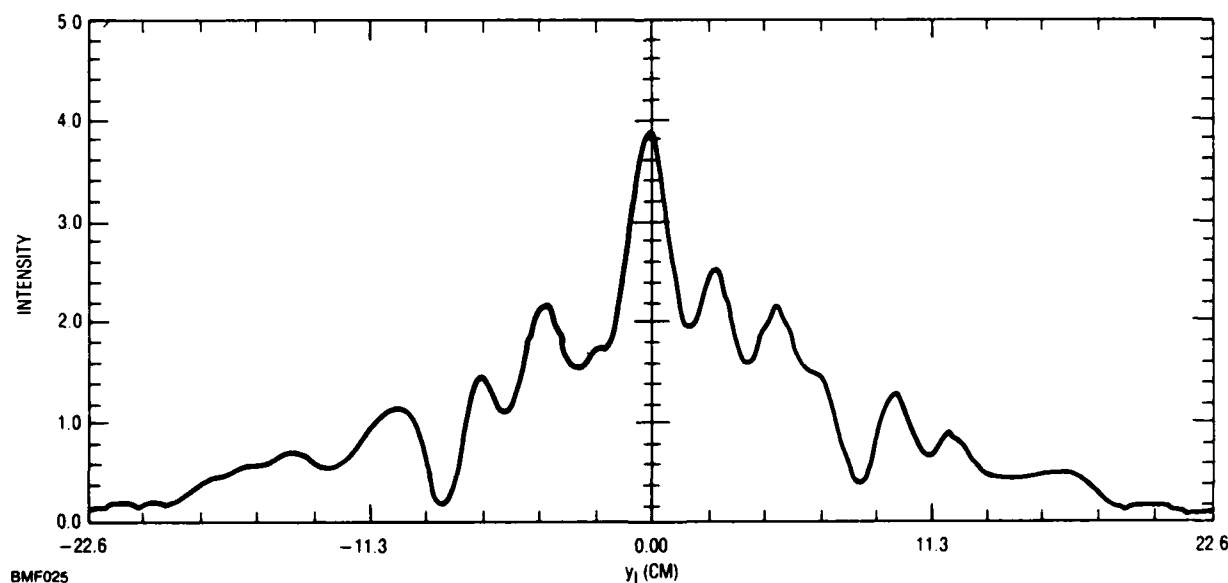


Figure 25. Intensity Produced by Summing Intensities for Four Spacings of Dielectric Waveguide Pair



## 8. SUMMARY

An approach to real-time microwave holographic imaging was studied. In particular, spatially noncoherent wavefront reconstruction methods were evaluated theoretically, numerically, and experimentally.

Spatially noncoherent reconstruction is done by doubling holograms; that is by forming two axially symmetric replicas of an original hologram. Axially symmetric pairs of points are coherent but not coherent with other pairs.

Two theoretical descriptions of the reconstruction are given. One theory assumes a hologram is formed and computes image intensity of the doubled hologram on the basis of array theory for the region of Fraunhofer diffraction, the farfield. The other theory also computes farfield image intensity, but it describes hologram formation for a point object and reference source; this theory involves integration over continuous apertures rather than discrete point sources as in array theory.

*The continuous theory can be interpreted physically to predict image locations. Both theories predict image locations that agree with measurement, but the discrete theory predicts magnitudes that more closely agree with measured values with a fiber optic doubler.*

Reconstruction experiments were done. No formation experiments were done to eliminate equipment costs; instead, previously formed holograms were used. The holograms were of a log periodic array radiating first in its sum mode and then in its difference mode. Wavelength was 3.30 cm.

Reconstructions were done with radiation of two distinct wavelengths.

Reconstructions were done with coherent infrared radiation from a line array of four 0.85 micrometer solid-state lasers, which replicated the hologram intensities. Holograms were doubled by directing the output of each laser to a pair of optical fibers. Reconstruction intensity was measured by an array of charge-coupled devices.

Reconstructions were also done with 8.57 mm waves. A pair of waveguides was connected to a signal generator. Interference fringe intensity was separately measured for four spacings of the radiating ends of the waveguides by scanning the image region with a small receiving antenna. The intensity for each spacing was stored in a computer and intensities for the four spacings were summed to effect noncoherent superposition.

The 0.85 micrometer reconstructions were described better by the discrete theory rather than the continuous; image locations were correct for both, but second-order image intensity was more accurate for the discrete theory. The continuous theory described the magnitudes of the millimeter wave reconstruction better than did the discrete theory. The apparent reason is in the width of hologram fringes compared to widths of radiating sources. That is, the element factor enters.

## 9. REFERENCES

1. G. L. Rogers, Nature 177, p. 613 (1956); J. Atm. Terr. Phys. 11, p. 51 (1957)
2. R. P. Dooley, Proc. IEEE 53, p. 1733 (1965)
3. G. Tricoles and E. L. Rope, J. Opt. Soc. Am. 56, p. 542A (1966); 57 p. 97 (1967)
4. Y. Aoki, Proc. IEEE 56, p. 1402 (1968)
5. R. D. Orme and A. P. Anderson, "High Resolution Microwave Holographic Technique," Proc. IEEE, 120, pp. 401-404 (1973)
6. O. C. Yue, E. L. Rope, and G. Tricoles, "Two Reconstruction Methods for Microwave Imaging of Buried Dielectric Anomalies," IEEE Trans. Comput., C-24, pp. 381-390 (1975)
7. R. A. Hayward et al., "Enhancement by Noncoherent Superposition of Microwave Images Formed with Crossed Coherent Arrays," in Acoustical Holography, N. O. Booth, ed. 6 pp. 469-484, New York: Plenum, 1975
8. Y. H. Ja, "Holographic Reconstruction of Source Distribution from Microwave Height Gain Curves," IEEE, Trans. Antennas Propagat. AP-24, pp. 1-5 (1976)
9. G. Tricoles and N. H. Farhart, "Microwave Holography: Techniques and Applications," Proc. IEEE 65, pp. 108-121 (1977)
10. G. Tricoles, E. L. Rope and R. A. Hayward, IEEE Trans. AP-29, pp. 320 (1981)
11. G. Tricoles, E. L. Rope, and R. A. Hayward, "Imaging Radio Wavesources with Two Spatially Noncoherent, Sparse Wavefront Sampling Arrays and Multiplicative Processing," in Proc. 10th Int. Opt. Comp. Conf., pp. 96-98, IEEE Cat. 83CH1880-4
12. R. O. Harger, Synthetic Aperture Radar Systems: Theory and Designs. (New York: Academic Press (1970))
13. L. J. Cutrona, W. E. Vivian, E. N. Leith, and G. O. Hall, "A High-Resolution Radar Combat Surveillance System," IRE Trans. Inform. Theory IT-6, pp. 386-400 (1961)

14. R. W. Larson, J. S. Zelenka, and E. L. Johansen, "A Microwave Hologram Radar System," IEEE Trans. Aerosp. Electron. Syst. AES-8, pp. 208-217 (1972)
15. Y. Rahmat-Samii, "Microwave Holography of Large Reflection Antennas," IEEE Trans. AP-33, pp. 1194 (1985)
16. G. Tricoles and R. A. Hayward, "Passive, Airborne Synthetic Holographic Imaging of Terrestrial Features With Radio Waves", 1986 National Radio Science Meeting
17. S. Y. Kung, "On Supercomputing with Systolic/Wavefront Array Processor," Proc IEEE 72, pp. 867-884 (1984)
18. G. Tricoles, E. Brundage, and E. L. Rope, "Wavefront Processing of Radio Frequency Wavefront Data", Proc. IEEE 72, pp. 885 (1984)
19. B. R. Brown and A. W. Lohmann, Appl. Opt. 6, p. 1739 (1967)

END

2-87

DTIC